

# Epitaxial Growth and Domain Structure Imaging of Kagome Magnet $\text{Fe}_3\text{Sn}_2$

Shuyu Cheng,<sup>\*</sup> Igor Lyalin,<sup>\*</sup> Alexander J. Bishop, and Roland K. Kawakami<sup>†</sup>  
*Department of Physics, The Ohio State University, Columbus, Ohio 43210, USA*

Magnetic materials with kagome crystal structure exhibit rich physics such as frustrated magnetism, skyrmion formation, topological flat bands, and Dirac/Weyl points. Until recently, most studies on kagome magnets have been performed on bulk crystals or polycrystalline films. Here we report the synthesis of high-quality epitaxial films of topological kagome magnet  $\text{Fe}_3\text{Sn}_2$  by atomic layer molecular beam epitaxy. Structural and magnetic characterization of  $\text{Fe}_3\text{Sn}_2$  on epitaxial Pt(111) identifies highly ordered films with c-plane orientation and an in-plane magnetic easy axis. Studies of the local magnetic structure by anomalous Nernst effect imaging reveals in-plane oriented micrometer size domains. The realization of high-quality films by atomic layer molecular beam epitaxy opens the door to explore the rich physics of this system and investigate novel spintronic phenomena by interfacing  $\text{Fe}_3\text{Sn}_2$  with other materials.

In recent years, studies on magnetic topological materials with kagome lattices have become one of the hottest frontiers of condensed matter research, due to their exotic physical properties in both real space and momentum space [1, 2]. In momentum space, angle-resolved photoemission spectroscopy (ARPES) experiments on  $\text{Mn}_3\text{Sn}$ ,  $\text{Fe}_3\text{Sn}_2$ ,  $\text{FeSn}$ , and  $\text{CoSn}$  [3–6] show that kagome lattices give rise to Dirac cones and flat bands which are topologically protected and are of particular interest. In addition, scanning tunneling spectroscopy finds evidence for topological flat bands as a sharp peak in the local density of states [7]. These topologically nontrivial features result in signatures of anomalous transport (e.g. chiral anomaly) in magnetotransport experiments [3, 8]. Furthermore, it is theoretically predicted that the band

structures of the kagome topological magnets can be controlled by tuning of their magnetic structures [1, 3]. In real space, the kagome topological magnets have layered structures with spins occupying corner-sharing triangular lattices, which leads to geometrical spin frustration [9, 10]. A surprisingly large anomalous Hall effect (AHE) and magneto-optic Kerr effect (MOKE) have been reported in noncollinear antiferromagnet  $\text{Mn}_3\text{Sn}$ , even with vanishingly small net magnetization [10, 11]. Skyrmion spin textures have been observed in ferromagnetic  $\text{Fe}_3\text{Sn}_2$  resulting from the competition of exchange, dipolar, and Zeeman energies [12, 13]. However, most of the studies on the kagome magnets have been done on bulk materials [4, 5, 10–16] with a few papers reporting the growth and characterization of epitaxial films [17–21]. Looking forward, epitaxial films will provide new opportunities for exploring fundamental physics and potential applications by tuning the dimensionality in thin films and interfacing  $\text{Fe}_3\text{Sn}_2$  with different materials. In addition, preparing and visualizing a well-defined domain structure is crucial for studying the spatially resolved physics of kagome magnets, such as spin transfer torque and spin-orbit torque induced domain wall and skyrmion motion [22, 23]. While the local magnetic structure of bulk  $\text{Fe}_3\text{Sn}_2$  has been recently studied and room temperature magnetic skyrmions were revealed [12, 13], there have been no studies probing the domain structure of  $\text{Fe}_3\text{Sn}_2$  in thin films.

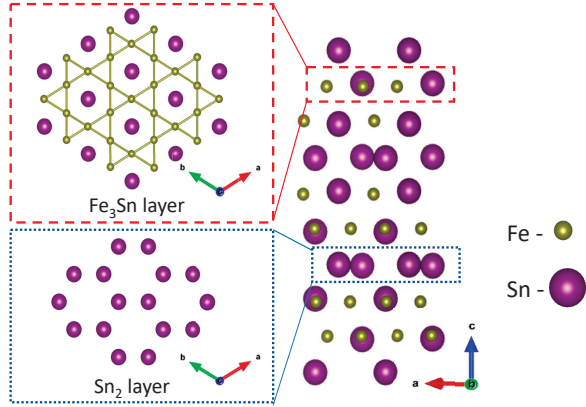


FIG. 1. Left: Top view of an individual  $\text{Fe}_3\text{Sn}$  layer with kagome structure (top) and  $\text{Sn}_2$  layer with honeycomb structure (bottom), respectively. Right: Side view of the crystal structure of  $\text{Fe}_3\text{Sn}_2$  consisting of alternating stacking of two  $\text{Fe}_3\text{Sn}$  kagome layers and one  $\text{Sn}_2$  layer.

<sup>\*</sup> These authors contributed equally.

<sup>†</sup> kawakami.15@osu.edu

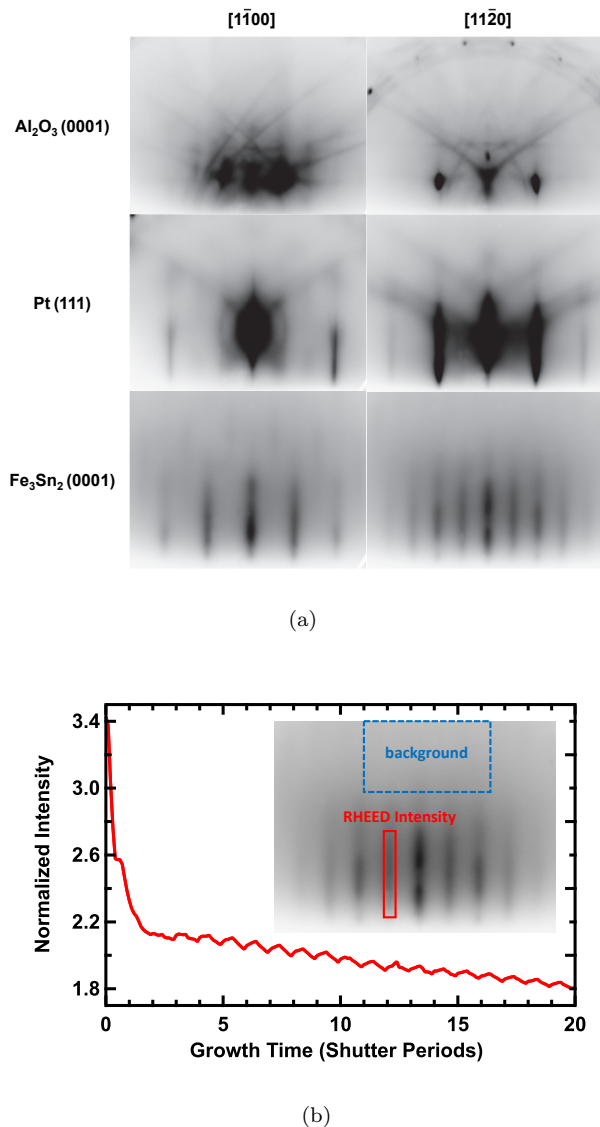


FIG. 2. (a) RHEED patterns for the  $\text{Al}_2\text{O}_3(0001)$  substrate, 5 nm Pt film, and 20 nm  $\text{Fe}_3\text{Sn}_2$  film measured with the beam along  $[1\bar{1}00]$  (left column) and  $[1\bar{1}20]$  (right column) directions of the substrate. (b) Oscillations in the normalized RHEED intensity as a function of time. The RHEED intensity is measured within the red box and normalized by the background in the blue box.

fully image the in-plane oriented domain structure of the epitaxial  $\text{Fe}_3\text{Sn}_2$  films and investigate the magnetization reversal as a function of applied field.

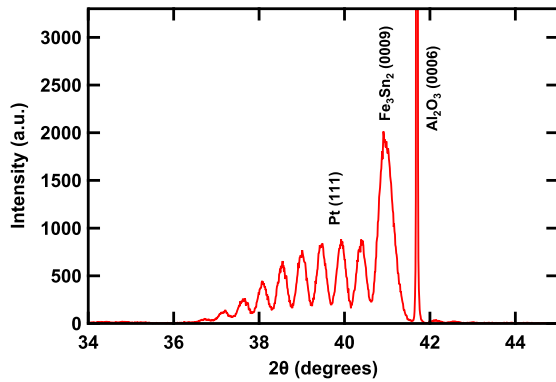
$\text{Fe}_3\text{Sn}_2$  is a ferromagnet with a high Curie temperature,  $T_C = 670$  K [24], and saturation magnetization of  $1.9 \mu_B$  per Fe at low temperature [4]. Fig. 1 shows the crystal structure of  $\text{Fe}_3\text{Sn}_2$  (space group  $R\bar{3}m$ , with lattice constants  $a = 5.338$  Å and  $c = 19.789$  Å [24]) which consists of  $\text{Fe}_3\text{Sn}$  kagome layers and Sn spacer layers. In each  $\text{Fe}_3\text{Sn}$  monolayer, the Fe atoms form corner-sharing equilateral triangles surrounding hexagons, with Sn atoms sitting in the center of the hexagons. The alter-

nating sequence of one  $\text{Sn}_2$  monolayer with honeycomb lattice and two  $\text{Fe}_3\text{Sn}$  kagome layers produces the layered crystal structure of  $\text{Fe}_3\text{Sn}_2$ .

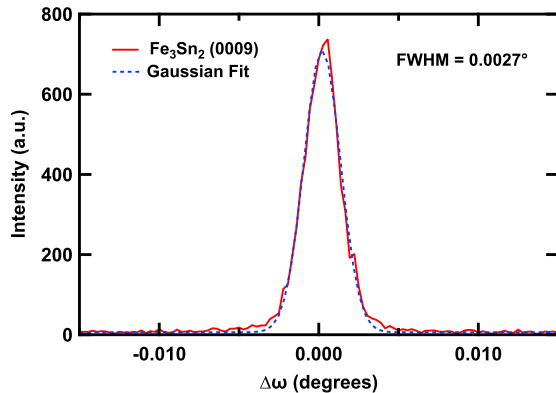
Based on this layered structure, we synthesized  $\text{Fe}_3\text{Sn}_2$  thin films on top of epitaxial Pt(111) buffer layers on  $\text{Al}_2\text{O}_3(0001)$  substrates by atomic layer MBE. The epitaxial growth was performed in an MBE chamber with a base pressure of  $4 \times 10^{-10}$  Torr. Films were deposited on  $\text{Al}_2\text{O}_3(0001)$  substrates (MTI Corporation) prepared by annealing in air at  $1000$  °C for 3 hours followed by annealing in ultrahigh vacuum (UHV) at  $500$  °C for 30 minutes. A 5 nm Pt(111) buffer layer was deposited from an e-beam evaporator (Pt: 99.99%, Kurt J. Lesker) onto the  $\text{Al}_2\text{O}_3(0001)$  substrate by growing the first 0.6 nm at  $440$  °C and the rest 4.4 nm while cooling down from  $140$  °C to  $80$  °C. The Pt buffer layer was post-annealed at  $300$  °C to improve the crystallinity and surface roughness. The  $\text{Fe}_3\text{Sn}_2$  layer was grown on Pt(111) at room temperature using the following atomic layer MBE sequence: deposit two atomic layers of  $\text{Fe}_3\text{Sn}$  with a Fe:Sn flux ratio of 3:1, deposit one atomic layer of  $\text{Sn}_2$  with the growth time same as two  $\text{Fe}_3\text{Sn}$  layers, then repeat. The Fe and Sn fluxes were generated from Knudsen cells (Fe: 99.99%, Alfa Aesar; Sn: 99.998%, Alfa Aesar) and the growth rates were determined using a quartz deposition monitor that was calibrated by x-ray reflectometry. Typical growth rates were  $\sim 0.85$  Å/min,  $\sim 0.67$  Å/min, and  $\sim 0.45$  Å/min for Fe, Sn, and Pt, respectively. To protect the sample from oxidation, a 3 nm Pt or 5 nm  $\text{CaF}_2$  capping layer was deposited on top of the  $\text{Fe}_3\text{Sn}_2$ .

RHEED patterns were measured during growth to characterize the epitaxial growth and determine the in-plane lattice constants. Figure 2a shows the RHEED patterns for the  $\text{Al}_2\text{O}_3(0001)$  substrate (top row), 5 nm Pt buffer layer (middle row), and the  $\text{Fe}_3\text{Sn}_2$  layer after 20 nm of growth (bottom row). The left and right columns show patterns taken for the beam along the  $[1\bar{1}00]$  and  $[1\bar{1}20]$  directions of the substrate, respectively. With in-plane rotation of the sample, RHEED exhibits the same pattern every  $60^\circ$  (i.e. six-fold rotation symmetry) with the patterns alternating between  $[1\bar{1}00]$ -type and  $[1\bar{1}20]$ -type every  $30^\circ$ . For the in-plane epitaxial alignment, the Pt(111) and  $\text{Fe}_3\text{Sn}_2(0001)$  surface unit cells are aligned with each other and rotated  $30^\circ$  with respect to the the  $\text{Al}_2\text{O}_3(0001)$  substrate, as  $a_{\text{Al}_2\text{O}_3} \approx (\sqrt{3}/2)2a_{\text{Pt}} \approx (\sqrt{3}/2)a_{\text{Fe}_3\text{Sn}_2}$  (bulk values for in-plane lattice constant are  $a_{\text{Al}_2\text{O}_3} = 4.759$  Å,  $2a_{\text{Pt}} = 5.549$  Å,  $a_{\text{Fe}_3\text{Sn}_2} = 5.338$  Å).

The streaky patterns observed during  $\text{Fe}_3\text{Sn}_2$  growth signify diffraction from a two-dimensional surface. In addition, we observe oscillations (Fig. 2b) in the normalized RHEED intensity where the maxima occurs for the  $\text{Fe}_3\text{Sn}$  termination and the minima occurs for the  $\text{Sn}_2$  termination. The normalization is performed by dividing the intensity of the background and is helpful for canceling variations in the incident beam intensity and background lighting. Except for the change in RHEED intensity, we did not observe any other significant dif-



(a)

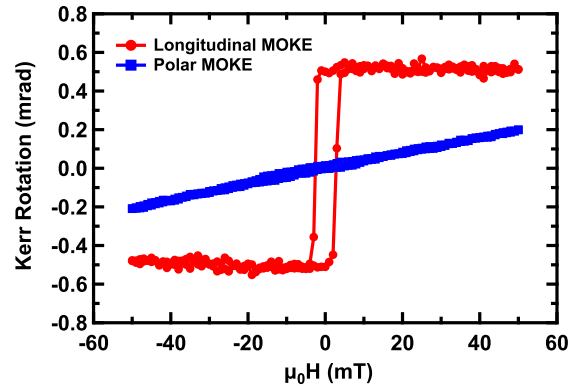


(b)

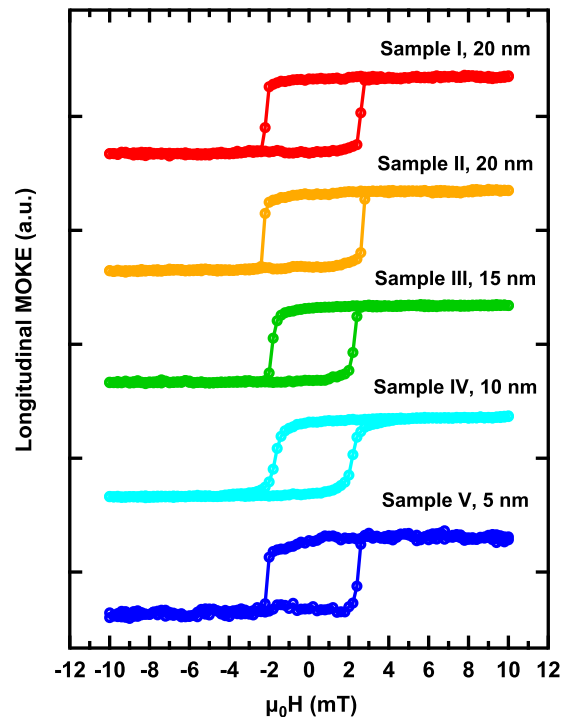
FIG. 3. (a)  $2\theta$ - $\omega$  scan of a 20 nm  $\text{Fe}_3\text{Sn}_2$  film grown on c-sapphire. (b) A triple axis  $\omega$ -relative scan (rocking curve) of the  $\text{Fe}_3\text{Sn}_2$  (009) peak (red) with a Gaussian fitting (blue).

ferences in the RHEED pattern between  $\text{Sn}_2$  and  $\text{Fe}_3\text{Sn}$  terminations. Nevertheless, the presence of RHEED oscillations in atomic layer MBE confirms the modulation of the surface termination during growth.

Films grown by this method were studied with XRD to analyze their crystal structure. A representative  $\omega$ - $2\theta$  scan of a 20 nm film is shown in Figure 3a and includes the  $\text{Fe}_3\text{Sn}_2$  (0009) peak with several Laue-oscillations, indicating a high degree of film smoothness. The out-of-plane lattice parameter extracted from analysis of this scan is 19.84 Å which agrees well with previous reports of 19.789 Å [24]. A peak from the 5 nm Pt(111) buffer layer produces a shoulder on the  $\text{Fe}_3\text{Sn}_2$  peak. Larger range scans do not show additional peaks from the  $\text{Fe}_3\text{Sn}_2$  or any other materials. To further analyze the crystallinity of our films, rocking curve scans about the  $\text{Fe}_3\text{Sn}_2$  (0009) peak were taken and analyzed. By scanning the sample angle  $\omega$  while keeping the detector fixed, this characterizes the angular distribution of the (0001) orientation relative to the film normal within the x-ray spot. Figure 3b contains a rocking curve or  $\omega$ -relative scan of the  $\text{Fe}_3\text{Sn}_2$  using a triple-axis analyzer to achieve high resolution of the desired peak. Fitting the peak with a standard



(a)



(b)

FIG. 4. (a). Longitudinal (red) and polar (blue) MOKE hysteresis loops of a 20 nm  $\text{Fe}_3\text{Sn}_2$  film (Sample I). (b). Zoomed-in scans for five different samples with thicknesses ranging from 5 nm to 20 nm, showing similar magnetic properties. The data are normalized to the saturation values and offset for clarity.

Gaussian yields a full width half maximum (FWHM) of  $0.0027^\circ$ . Such a sharp peak indicates that films grown by atomic layer MBE have excellent mosaicity.

To investigate the in-plane and out-of-plane magnetic properties of the  $\text{Fe}_3\text{Sn}_2$  films, we measured longitudinal and polar MOKE hysteresis loops. The samples were probed using a linearly-polarized He-Ne laser (633 nm wavelength,  $\sim 100 \mu\text{W}$  power,  $\sim 100 \mu\text{m}$  spot size) and a polarizing beamsplitter, photodiode bridge, and lock-

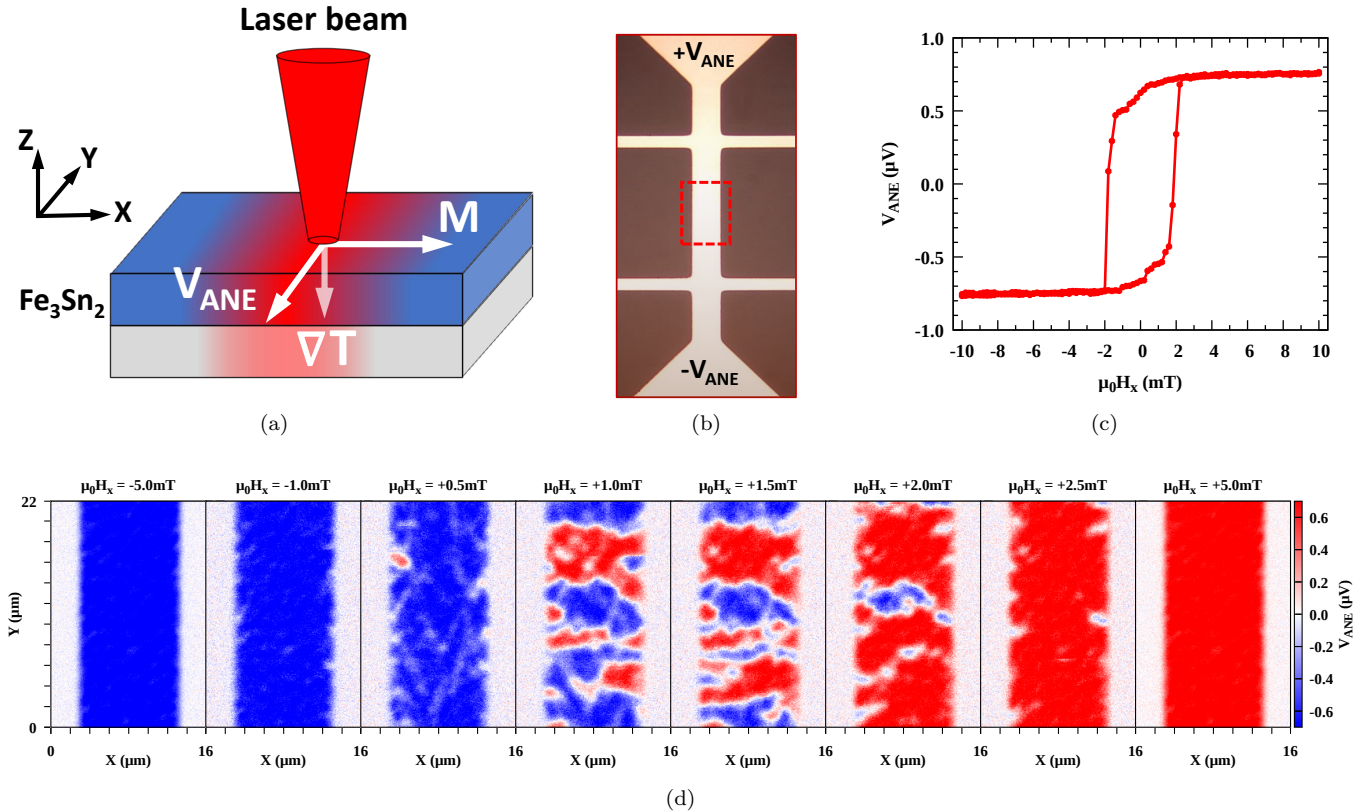


FIG. 5. (a) Schematics of thermal gradient microscopy. The laser beam is scanned over the sample surface, the induced local ANE voltage reflects the local magnetic properties. (b) Microscope image of a typical device, (the dashed rectangle corresponds to the area imaged in (d)) (c) ANE hysteresis loop of a 20 nm  $\text{Fe}_3\text{Sn}_2$  film. (d) Magnetization reversal of a 20 nm film through multidomain state imaged by ANE at a series of magnetic fields  $\mu_0 H_x$ .

in amplifier (463 Hz intensity modulation) to detect the Kerr rotation. The laser beam had a  $\sim 45^\circ$  angle of incidence for longitudinal MOKE and normal incidence for polar MOKE. Figure 4a shows a representative longitudinal hysteresis loop (red curve) measured on a 20 nm thick  $\text{Fe}_3\text{Sn}_2$  sample (Sample I). The square hysteresis loop with a coercivity of 2.4 mT indicates ferromagnetic order with in-plane magnetization. In contrast, the polar hysteresis loop (blue curve) shows a small Kerr rotation with slight variation with out-of-plane magnetic field. Together, the longitudinal and polar MOKE loops show that the  $\text{Fe}_3\text{Sn}_2$  samples have an easy-plane magnetic anisotropy. This agrees with a previous study of  $\text{Fe}_3\text{Sn}_2$  films grown by sputter deposition [20]. To check the consistency of the synthesis and magnetic properties, we investigated additional samples grown by the same method with thickness varying from 5 to 20 nm. The results are shown in Fig. 4b. All the samples show very similar magnetic properties, with square in-plane hysteresis loops and similar coercive fields.

The magnetic domain structure of  $\text{Fe}_3\text{Sn}_2$  films are of interest due to the observation of skyrmions in bulk  $\text{Fe}_3\text{Sn}_2$ , but has not yet been studied in thin films. Longitudinal MOKE microscopy with oblique angle incidence can detect the in-plane magnetization and therefore de-

termine in-plane domain structure of our  $\text{Fe}_3\text{Sn}_2$  films. However, in this manuscript, we choose to use thermal gradient microscopy (TGM) [25–27] over longitudinal MOKE to image domain structure because we found that it has a better signal-to-noise ratio in our experimental setup.

TGM is based on moving a laser spot over the sample surface, and recording a voltage induced by the local laser heating. The thermal gradient generated in the out-of-plane direction  $Z$  and a component of magnetization in the  $X$  direction give rise to the anomalous Nernst effect, which is detected as a voltage along the  $Y$  direction,  $V_{ANE} \sim [\nabla T \times \mathbf{M}]$  (see Fig. 5a).

For the ANE imaging, we fabricated 10  $\mu\text{m}$  wide Hall bar devices by a combination of photolithography and argon ion milling (Fig. 5b). The laser excitation for the thermal gradient was produced by a frequency-doubled ( $\text{BaB}_2\text{O}_4$  crystal) mode-locked Ti:Sapphire laser for a wavelength of 400 nm. The laser beam with 0.7 mW power was focused by a 50 $\times$  objective lens (NA of 0.6) to a spot size of 0.9  $\mu\text{m}$ , and a fast steering mirror in the 4f alignment scheme was used for scanning the laser spot over the sample surface. The intensity of the beam was modulated at a frequency of 120 kHz and the generated ANE voltage was detected using a lock-in amplifier.

We first utilized the ANE microscope to measure a detailed hysteresis loop at a fixed position. As shown in Fig. 5c for magnetic field along the  $X$  direction, the hysteresis loop shows a gradual reversal followed by a sharp switching behavior with coercivity of 1.9 mT. This has a similar coercivity but more gradual initial reversal than the in-plane hysteresis loops obtained by MOKE (Fig. 4b).

The origin of the different hysteresis properties is revealed by imaging the magnetic domain structure of  $\text{Fe}_3\text{Sn}_2$  films at a series of magnetic fields. A representative sequence during the magnetization reversal is shown in Fig. 5d. Starting at -5.0 mT, the magnetization is in a saturated state along  $-X$  (blue). The reversal initiates with the nucleation of white regions with  $M_x \approx 0$ , mainly at the edges of the sample. This can be explained by the minimization of domain wall energy as the edge boundary does not contribute a domain wall energy cost. The nucleation at the edges initiates magnetization reversal which results in a more rounded hysteresis loop compared to the uniform films. With increasing magnetic field, domains of opposite polarity grow inward and coalesce across the channel. At about +1.0 mT, the magnetic structure is in a multidomain state with characteristic features (e.g. blue and red regions) ranging from 1 to 10 microns in size. By +2.0 mT, most of the magnetic moments have switched to  $+X$  direction, with only a few regions remaining along  $-X$ . Finally, at +5.0 mT the magnetization reversal is complete and the films is fully saturated along  $+X$ .

In conclusion, we report the growth and characterization of kagome ferromagnet  $\text{Fe}_3\text{Sn}_2$  thin films on

$\text{Pt}(111)/\text{Al}_2\text{O}_3(0001)$  by atomic layer molecular beam epitaxy. Structural characterization by *in situ* RHEED and XRD confirm the high quality of the epitaxial  $\text{Fe}_3\text{Sn}_2$  films. The magnetic properties were investigated by magneto-optical Kerr effect and anomalous Nernst effect, confirming the easy-plane magnetic anisotropy of the thin films. Finally, the local magnetic structure was probed by ANE microscopy revealing the presence of in-plane oriented micrometer size domains during magnetization reversal. These results highlight the potential for epitaxial growth to enable new scientific research in kagome magnets at the intersection of topology and magnetism.

## ACKNOWLEDGEMENTS

S.C., I.L., and R.K.K. acknowledge support from DARPA Grant No. D18AP00008. A.J.B. and R.K.K. acknowledge support from DOE Grant No. DE-SC0016379. This research was partially supported by the Center for Emergent Materials, an NSF MRSEC, under award number DMR-2011876.

## AUTHOR CONTRIBUTIONS

S.C., I.L., and R.K.K. conceived the experiments. S.C. conducted the MBE growth and MOKE measurements. I.L. conducted the ANE measurements. A.J.B. conducted the XRD measurements. All authors participated in data analysis and preparation of the manuscript.

- 
- [1] L. Šmejkal, Y. Mokrousov, B. Yan, and A. H. MacDonald, Topological antiferromagnetic spintronics, *Nature Physics* **14**, 242 (2018).
  - [2] H. Yang, Y. Sun, Y. Zhang, W.-J. Shi, S. S. Parkin, and B. Yan, Topological weyl semimetals in the chiral antiferromagnetic materials  $\text{Mn}_3\text{Ge}$  and  $\text{Mn}_3\text{Sn}$ , *New Journal of Physics* **19**, 015008 (2017).
  - [3] K. Kuroda, T. Tomita, M.-T. Suzuki, C. Bareille, A. A. Nugroho, P. Goswami, M. Ochi, M. Ikhlas, M. Nakayama, S. Akebi, R. Noguchi, R. Ishii, N. Inami, K. Ono, H. Kumigashira, A. Varykhalov, T. Muro, T. Koretsune, R. Arita, S. Shin, T. Kondo, and S. Nakatsuji, Evidence for magnetic Weyl fermions in a correlated metal, *Nature Materials* **16**, 1090 (2017).
  - [4] L. Ye, M. Kang, J. Liu, F. von Cube, C. R. Wicker, T. Suzuki, C. Jozwiak, A. Bostwick, E. Rotenberg, D. C. Bell, L. Fu, R. Comin, and J. G. Checkelsky, Massive Dirac fermions in a ferromagnetic kagome metal, *Nature* **555**, 638 (2018).
  - [5] M. Kang, L. Ye, S. Fang, J.-S. You, A. Levitan, M. Han, J. I. Facio, C. Jozwiak, A. Bostwick, E. Rotenberg, M. K. Chan, R. D. McDonald, D. Graf, K. Kaznatcheev, E. Vescovo, D. C. Bell, E. Kaxiras, J. van den Brink, M. Richter, M. Prasad Ghimire, J. G. Checkelsky, and R. Comin, Dirac fermions and flat bands in the ideal kagome metal  $\text{FeSn}$ , *Nature Materials* **19**, 163 (2020).
  - [6] M. Kang, S. Fang, L. Ye, H. C. Po, J. Denlinger, C. Jozwiak, A. Bostwick, E. Rotenberg, E. Kaxiras, J. G. Checkelsky, and R. Comin, Topological flat bands in frustrated kagome lattice  $\text{CoSn}$ , *Nature Communications* **11**, 4004 (2020).
  - [7] J.-X. Yin, S. S. Zhang, G. Chang, Q. Wang, S. S. Tsirkin, Z. Guguchia, B. Lian, H. Zhou, K. Jiang, I. Belopolski, N. Shumiya, D. Multer, M. Litskevich, T. A. Cochran, H. Lin, Z. Wang, T. Neupert, S. Jia, H. Lei, and M. Z. Hasan, Negative flat band magnetism in a spin-orbit-coupled correlated kagome magnet, *Nature Physics* **15**, 443 (2019).
  - [8] T. Chen, T. Tomita, S. Minami, M. Fu, T. Koretsune, M. Kitatani, I. Muhammad, D. Nishio-Hamane, R. Ishii, F. Ishii, R. Arita, and S. Nakatsuji, Anomalous transport due to Weyl fermions in the chiral antiferromagnets  $\text{Mn}_3\text{X}$ ,  $\text{X} = \text{Sn}, \text{Ge}$ , *Nature Communications* **12**, 572 (2021).
  - [9] L. Fenner, A. Dee, and A. Wills, Non-collinearity and spin frustration in the itinerant kagome ferromagnet  $\text{Fe}_3\text{Sn}_2$ , *Journal of Physics: Condensed Matter* **21**, 452202 (2009).



- [10] S. Nakatsuji, N. Kiyohara, and T. Higo, Large anomalous Hall effect in a non-collinear antiferromagnet at room temperature, *Nature* **527**, 212 (2015).
- [11] T. Higo, H. Man, D. B. Gopman, L. Wu, T. Koretsune, O. M. J. van 't Erve, Y. P. Kabanov, D. Rees, Y. Li, M.-T. Suzuki, S. Patankar, M. Ikhlas, C. L. Chien, R. Arita, R. D. Shull, J. Orenstein, and S. Nakatsuji, Large magneto-optical Kerr effect and imaging of magnetic octupole domains in an antiferromagnetic metal, *Nature Photonics* **12**, 73 (2018).
- [12] Z. Hou, W. Ren, B. Ding, G. Xu, Y. Wang, B. Yang, Q. Zhang, Y. Zhang, E. Liu, F. Xu, W. Wang, G. Wu, X. Zhang, B. Shen, and Z. Zhang, Observation of Various and Spontaneous Magnetic Skyrmionic Bubbles at Room Temperature in a Frustrated Kagome Magnet with Uniaxial Magnetic Anisotropy, *Advanced Materials* **29**, 1701144 (2017).
- [13] Z. Hou, Q. Zhang, G. Xu, S. Zhang, C. Gong, B. Ding, H. Li, F. Xu, Y. Yao, E. Liu, G. Wu, X.-x. Zhang, and W. Wang, Manipulating the Topology of Nanoscale Skyrmion Bubbles by Spatially Geometric Confinement, *ACS Nano* **13**, 922 (2019).
- [14] L. A. Fenner, A. A. Dee, and A. S. Wills, Non-collinearity and spin frustration in the itinerant kagome ferromagnet  $\text{Fe}_3\text{Sn}_2$ , *J. Phys.: Condens. Matter* **21**, 452202 (2009).
- [15] T. Kida, L. A. Fenner, A. A. Dee, I. Terasaki, M. Hagiwara, and A. S. Wills, The giant anomalous Hall effect in the ferromagnet  $\text{Fe}_3\text{Sn}_2$ —a frustrated kagome metal, *J. Phys.: Condens. Matter* **23**, 112205 (2011).
- [16] A. K. Nayak, J. E. Fischer, Y. Sun, B. Yan, J. Karel, A. C. Komarek, C. Shekhar, N. Kumar, W. Schnelle, J. Kübler, C. Felser, and S. S. P. Parkin, Large anomalous Hall effect driven by a nonvanishing Berry curvature in the noncolinear antiferromagnet  $\text{Mn}_3\text{Ge}$ , *Science Advances* **2**, e1501870 (2016).
- [17] A. Markou, J. M. Taylor, A. Kalache, P. Werner, S. S. P. Parkin, and C. Felser, Noncollinear antiferromagnetic  $\text{Mn}_3\text{Sn}$  films, *Phys. Rev. Materials* **2**, 051001 (2018).
- [18] H. Inoue, M. Han, L. Ye, T. Suzuki, and J. G. Checkelsky, Molecular beam epitaxy growth of antiferromagnetic Kagome metal  $\text{FeSn}$ , *Appl. Phys. Lett.* **115**, 072403 (2019).
- [19] J. M. Taylor, A. Markou, E. Lesne, P. K. Sivakumar, C. Luo, F. Radu, P. Werner, C. Felser, and S. S. P. Parkin, Anomalous and topological Hall effects in epitaxial thin films of the noncollinear antiferromagnet  $\text{Mn}_3\text{Sn}$ , *Phys. Rev. B* **101**, 094404 (2020).
- [20] D. Khadka, T. R. Thapaliya, S. Hurtado Parra, J. Wen, R. Need, J. M. Kikkawa, and S. X. Huang, Anomalous Hall and Nernst effects in epitaxial films of topological kagome magnet  $\text{Fe}_3\text{Sn}_2$ , *Phys. Rev. Materials* **4**, 084203 (2020).
- [21] D. Hong, C. Liu, H.-W. Hsiao, D. Jin, J. E. Pearson, J.-M. Zuo, and A. Bhattacharya, Molecular beam epitaxy of the magnetic kagome metal  $\text{FeSn}$  on  $\text{LaAlO}_3(111)$ , *AIP Advances* **10**, 105017 (2020).
- [22] S. S. P. Parkin, M. Hayashi, and L. Thomas, Magnetic Domain-Wall Racetrack Memory, *Science* **320**, 190 (2008).
- [23] A. Fert, N. Reyren, and V. Cros, Magnetic skyrmions: advances in physics and potential applications, *Nature Reviews Materials* **2**, 1 (2017).
- [24] H. Giefers and M. Nicol, High pressure X-ray diffraction study of all Fe–Sn intermetallic compounds and one Fe–Sn solid solution, *Journal of Alloys and Compounds* **422**, 132 (2006).
- [25] M. Weiler, M. Althammer, F. D. Czeschka, H. Huebl, M. S. Wagner, M. Opel, I.-M. Imort, G. Reiss, A. Thomas, R. Gross, and S. T. B. Goennenwein, Local Charge and Spin Currents in Magnetothermal Landscapes, *Phys. Rev. Lett.* **108**, 106602 (2012).
- [26] I. Gray, T. Moriyama, N. Sivadas, G. M. Stiehl, J. T. Heron, R. Need, B. J. Kirby, D. H. Low, K. C. Nowack, D. G. Schlom, D. C. Ralph, T. Ono, and G. D. Fuchs, Spin Seebeck Imaging of Spin-Torque Switching in Antiferromagnetic Pt/NiO Heterostructures, *Phys. Rev. X* **9**, 041016 (2019).
- [27] H. Reichlova, T. Janda, J. Godinho, A. Markou, D. Kriegner, R. Schlitz, J. Zelezny, Z. Soban, M. Bejarano, H. Schultheiss, P. Nemeč, T. Jungwirth, C. Felser, J. Wunderlich, and S. T. B. Goennenwein, Imaging and writing magnetic domains in the non-collinear antiferromagnet  $\text{Mn}_3\text{Sn}$ , *Nature Communications* **10**, 5459 (2019).